

Hidden soils and their carbon stocks at high-elevation in the European Alps (North-West Italy)

Original

Hidden soils and their carbon stocks at high-elevation in the European Alps (North-West Italy) / Pintaldi, E., D'Amico, M.E., Colombo, N., Colombero, C., Sambuelli, L., De Regibus, C., Franco, D., Perotti, L., Paro, L., Freppaz, M.. - In: CATENA. - ISSN 0341-8162. - ELETTRONICO. - 198:(2021). [10.1016/j.catena.2020.105044]

Availability:

This version is available at: 11583/2854427 since: 2020-12-02T14:28:27Z

Publisher:

Elsevier B.V.

Published

DOI:10.1016/j.catena.2020.105044

Terms of use:

This article is made available under terms and conditions as specified in the corresponding bibliographic description in the repository

Publisher copyright

(Article begins on next page)

1 **Hidden soils and carbon stocks in high-elevation ecosystems in the** 2 **Alps (NW-Italy)**

3

4 Emanuele Pintaldi^{1,*}, Michele E. D'Amico¹, Nicola Colombo^{1,2,3}, Chiara Colombero⁴, Luigi
5 Sambuelli⁴, Claudio De Regibus⁴, Diego Franco⁴, Luigi Perotti³, Michele Freppaz^{1,2}

6

7 ¹University of Turin, Department of Agricultural, Forest and Food Sciences (DISAFA), Largo
8 Braccini, 2, 10095 Grugliasco (TO), Italy.

9 ²University of Turin, Research Center on Natural Risk in Mountain and Hilly Environments
10 (NatRisk), Largo Braccini, 2, 10095 Grugliasco (TO), Italy.

11 ³University of Turin, Department of Earth Sciences (DST), Via Valperga Caluso, 35, 10125 Turin,
12 Italy.

13 ⁴Politecnico di Torino, Department of Environment, Land and Infrastructure Engineering (DIATI),
14 Corso Duca degli Abruzzi, 24, 10129 Turin, Italy.

15

16 **Abstract**

17 Alpine soils, especially those covered by vegetation and/or with permafrost, store large quantities of
18 total organic carbon (TOC). Given their high vulnerability to climate change, they may release large
19 amounts of CO₂ in a warming scenario. Thus, it is important to know their C stock in order to
20 understand its possible release. While C stocks of forest and alpine grassland soils are well
21 documented, little is known about soils and C stocks in high-elevated periglacial environments
22 dominated by cryoturbation. The object of this study is the periglacial environment of the
23 Stolenberg Plateau (LTER site Istituto Mosso, 3030 m a.s.l.), at the foot of the Monte Rosa Massif
24 (NW Italian Alps). The plateau is covered by a thick stony layer, organized in periglacial
25 blockfields and blockstreams. The plant cover reaches only 3-5%. During the construction of a chair

26 lift, the opening of trenches revealed, unexpectedly, extremely well-developed soils under the active
27 periglacial stone cover. In particular, thick (30-65 cm) and dark TOC-rich A horizons were
28 observed. Below these umbric horizons, cambic Bw ones were developed but discontinuous.
29 Despite the lack of vegetation, C stocks were surprisingly high (up to $\sim 5 \text{ kg} \cdot \text{m}^{-2}$), comparable to
30 vegetated soils at lower elevation. Non-invasive geophysical methods revealed that these hidden
31 soils were widespread on the plateau under the stony cover, with a mean thickness around 50 cm.
32 These TOC-rich soils, without vegetation and covered by periglacial landforms, represent a unique
33 pedoenvironment suggesting new perspectives on the actual C-stocks in high-elevation ecosystems,
34 which are probably underestimated.

35

36 **Keywords**

37 Soil organic matter; Periglacial; Blockstream/Blockfield; Geophysics

38 **1 Introduction**

39 Soil Organic Matter (SOM) stored in alpine soils is a fundamental part of the global C cycle
40 (Prietzl and Christophel, 2014), acting as a sink for carbon dioxide and having therefore a great
41 potential to sequester this from the atmosphere (Bojko and Kabala, 2017). Alpine soils, especially
42 those covered by vegetation and/or with permafrost, store large quantities of organic carbon (e.g.,
43 Celi et al., 2010; Bockheim and Munroe, 2014). However, given the high vulnerability of soils to
44 climate change (Schröter et al., 2005; Hagedorn et al., 2010), they may release large amounts of
45 carbon dioxide in a warming scenario (e.g., Schuur et al., 2013; Knowles et al., 2019).

46 High-elevation soils are dominated by cryoturbation processes, induced by seasonal frost
47 penetration or permafrost, leading to the formation of patterned ground, typical of periglacial
48 environments (e.g., tilting of stones, blockstreams, blockfield, wedges, etc.). As it is mostly driven
49 by temperature, active patterned ground is vulnerable to climate warming, which can induce several
50 possible effects such as permafrost degradation (e.g., Biskaborn et al., 2019; Mollaret et al., 2019),

51 expansion of plant cover and transition from pioneer species towards more acidophilous grassland
52 (e.g., Gerdol and Smiraglia, 1990; D'Amico et al., 2015), and increased SOM decomposition (e.g.,
53 Álvarez Arteaga et al., 2008; Cheng et al., 2012).

54 While the carbon stocks of forest and alpine grassland soils are well documented by several studies
55 (e.g., Leifeld et al., 2009; Zollinger et al., 2013; Bockheim and Munroe, 2014), very little is known
56 about carbon stocks in high-elevated periglacial environments, especially in the European Alps.
57 This is probably due to different reasons, such as: 1) these soils are located in very unfavourable
58 conditions at high elevation and they are often difficult to reach, requiring specific technical
59 equipment; 2) generally, these high-elevation surfaces are not covered by vegetation therefore,
60 considering plants as first carbon source, these soils received less interest since they are not
61 considered a relevant carbon sink compared to forest soils; 3) high-elevation soils are typical of
62 periglacial environments, which are characterized by cryoturbation processes (induced by low
63 temperatures and/or permafrost) that allow the formation of patterned ground. Thus, they are
64 frequently covered by coarse debris which makes it difficult to recognize them as soils and perform
65 in-depth pedological investigations using manual devices.

66 In order to deepen the investigation on these high-elevation pedoenvironments, geophysical
67 methods can be used thanks to their capability to map soil thickness and distribution even in areas
68 of intricate relationships between soil and top or bottom enclosing geological materials, undulating
69 topography, and non-homogeneous or anisotropic material properties. Among the available
70 geophysical methods, Electrical Resistivity Tomography (ERT) allows investigating contrasts in
71 electrical properties between the soil material (loose, porous, prone to water retention and possibly
72 rich in organic matter) and massive bedrock or coarse glacial deposits. The same contrast in
73 physical and mechanical properties, together with differences in layering and internal structure, can
74 be imaged using Ground Penetrating Radar (GPR) profiling. ERT and GPR are widely used to
75 support pedological surveys for soil classification, mapping of the presence, depth and lateral
76 variability of soil horizons, agricultural purposes and contamination analyses from low to mid

77 latitudes and elevations (e.g., Samouelian et al., 2005; Allred et al., 2008; Doolittle and Butnor,
78 2009; Andre et al., 2012; Nováková et al., 2013). By contrast, few applications of geophysical
79 prospections for the study of high-elevation soils are reported in the literature. In periglacial
80 environments, these techniques are mainly used for permafrost characterization, hydrogeological
81 processes and soil-bedrock interface recognition (Moorman et al., 2003; Otto and Sass, 2006;
82 Kneisel et al. 2008; McClymont et al., 2010; Léger et al., 2017).

83 The study area is located in the severe periglacial environment of the Stolenberg Plateau (3030 m
84 a.s.l., LTER site Istituto Mosso) on the southern slope of Monte Rosa Massif (4634 m a.s.l., NW
85 Italian Alps) where, in 2017, the operational activities for a new chair lift construction inside a
86 blockfield/blockstream area revealed unexpected well-developed soils. Considering the
87 impossibility to deepen the investigation using manual devices and machinery, and the necessity to
88 detect the distribution of these hidden soils, non-invasive geophysical methods were applied in
89 September 2019.

90 Based on previous considerations, this work aims at: 1) describing and classifying the buried soils,
91 2) evaluating their carbon stock, and 3) investigating their distribution and thickness.

92

93

94 **2 Materials and Methods**

95 **2.1 Study Area**

96 The work was carried out in the periglacial environment of the Stolenberg Plateau, located at 3030
97 m a.s.l., at the boundary between Valle d’Aosta and Piemonte regions (Fig. 1), at the foot of the
98 southern slope of Monte Rosa (4634 m) (NW Italian Alps). The research area represents the summit
99 portion of the Long Term Ecological Research (LTER) site Angelo Mosso Scientific Institute
100 (LTER-Italia IT19-001-T), belonging to the LTER-Italy network. The study area is also a Site of
101 Community Importance and a Special Protection Area (SCI/SPA IT1204220 “Ambienti glaciali del
102 gruppo del Monte Rosa”) (Directive, 1992) belonging to the Natura 2000 network.

103 From 2007 to 2018, the area had a mean annual air temperature of -2.3 °C, a mean cumulative
104 annual snowfall of 818 cm, and a mean annual liquid precipitation of ca. 400 mm. Snow cover lasts
105 for at least 8 months, reaching a maximum thickness of ca. 350 cm (Freppaz et al., 2019).
106 During the snow-free season, the area shows typical features of periglacial environments,
107 characterized by active periglacial landforms. In particular, the plateau is covered by a thick layer of
108 stones with variable size (from decimetric to metric), well organized in blockfields,
109 blockstreams/sorted stripes, gelifluction lobes, tilted stones and weakly developed sorted circles
110 (Fig. 1). The activity of the morphology is evidenced by the absence of lichens from most stones
111 (Ballantyne and Matthews, 1982). The parent material is composed of gneiss and mica-schists
112 (Monte Rosa nappe, Penninic basement) and metabasites (Zermatt-Saas unit).
113 The vegetation cover, which is almost absent or confined to small patches reaching no more than
114 5% of the plateau areal extension, is composed mainly of alpine species such as *Silene acaulis*,
115 *Carex curvula*, *Salix herbacea* in the vegetated patches, while *Festuca halleri*, *Poa alpina*,
116 *Ranunculus glacialis*, *Leuchanemopsis alpina*, *Cerastium uniflorum* and a few other pioneer
117 species grow also in the stone-covered area, with extremely low cover values.

118

119 **2.2 Soil survey sampling and analysis**

120 In 2017, during the operational activities for a new chair lift construction, the largest part of the
121 plateau was delimited in order to protect the natural environment (Directive, 1992) and the
122 periglacial features from the excavation operations. However, three trenches were opened (2-10 m
123 long, to a depth of around 1.2 m) in the construction area, revealing unexpected, well-developed
124 soils under the stony cover. This finding was possible only thanks to the machinery employed,
125 which utilization was exceptionally allowed for the construction of the chair lift station.
126 Field description of soils transect was performed according to FAO (2006), while soil classification
127 was done according to WRB classification system (FAO, 2014). Three soil profiles were described
128 and sampled, named P1, P2 and P3 (Fig. 1). Overall, 27 soil samples were collected from the

129 profiles. The samples were air-dried, sieved to 2 mm and analyzed following the standard methods
130 reported by Van Reeuwijk (2002). The pH was measured in water (soil: water = 1:2.5). The
131 particle-size analysis was performed by the pipette method after organic matter destruction with
132 H₂O₂ followed by dispersion with Na-hexametaphosphate. Total carbon (corresponding to total
133 organic carbon-TOC due to the absence of carbonates) and nitrogen (TN) concentrations, were
134 measured by dry combustion with an elemental analyzer (CE Instruments NA2100, Rodano, Italy).
135 The soil organic carbon stock (C-STOCK_{tot} kg*m⁻²) of the profiles was calculated for sectors in
136 which the horizons sequence was similar, according to the following equation adapted from Batjes
137 (1996):

$$138 \quad C - STOCK_{tot} = \sum_{i=1}^n \frac{TOC * BD * TH * VF}{1000} \quad (1)$$

139 where n is the number of soil horizons of each sector, TOC is the soil organic carbon concentration
140 (g*kg⁻¹) of the mineral horizons, BD is the Bulk Density (kg*m⁻³) based on mean Bulk Density
141 values of high-elevation soils (D'Amico et al., submitted) measured according to Boone et al.
142 (1999), TH is the horizon thickness (m), VF is the volume of fine earth excluding the coarse
143 mineral fraction (> 2 mm), calculated as [1 - (% rock volume/100)], 1000 is the unit correction
144 factor.

145 In order to support the interpretation of the geophysical measurements, the clay mineralogy was
146 analysed using a Philips PW1710 X-ray diffractometer (40kV and 20 mA, CoK α radiation, graphite
147 monochromator). The Mg saturated clay fraction (< 2 μ m) was separated by sedimentation,
148 flocculated with MgCl₂, washed until free of Cl⁻, and freeze-dried. Scans were made from 3 to 35
149 $^{\circ}2\theta$ at a speed of 1 $^{\circ}2\theta$ min⁻¹, on air dried, ethylene glycol solvated, and heated (350 $^{\circ}$ and 550 $^{\circ}$ C)
150 oriented mounts. A semi-quantitative evaluation of mineral abundance was performed using the
151 Mineral Intensity Factors method (Islam and Lotse, 1986), which considers peak areas. For the
152 calculation, the background was subtracted and the peak positions, intensities and areas were
153 calculated using the PowderX software (Dong, 1999).

155 **2.3 Geophysical investigation**

156 Six 48-electrode Electrical Resistivity Tomography (ERT) profiles were acquired (Fig. 1). Five of
157 them had an inter-electrode spacing of 0.30 m, for a total length of 14.1 m. One longer profile (ERT
158 3 in Fig. 1) was acquired with a spacing of 2 m between the electrodes, for a total length of 94 m.
159 Short profiles were aimed at the detection and lateral imaging at shallow depths of the buried soils
160 with high-resolution, while the longer line was designed for a deeper general low-resolution
161 characterization of the bedrock conditions on which the soil horizons lay. Electrodes were
162 georeferenced using a Garmin GPS 60 system to retrieve the position of each survey line on a high-
163 resolution digital surface model (DSM) of the plateau and later account for topographic variations
164 in the inversion of the longest ERT line, for which differences in height between the electrodes
165 were significant. Digital vertical and slantwise photos obtained from an Unmanned Aerial Vehicle
166 (UAV) survey were processed with structure from motion and multi-view-stereo algorithms to
167 produce a high-resolution DSM (10 cm / pixel ground resolution) of the investigated area (cf.,
168 Smith et al. 2015; Carrivick et al., 2016, Alberto et al., 2018) (Supplementary Material, SM1).
169 ERT data were acquired with a multichannel resistivity meter (Syscal Pro - Iris Instruments). The
170 acquisition scheme included 870 Wenner-Schlumberger array configurations along each line. On
171 each quadrupole, measurements were repeated between 5 and 10 times, to reach a standard
172 deviation of the average measured values lower than 5%. Raw data were manually filtered basing
173 on their related standard deviation and inverted with Res2DInv software (Loke and Barker, 1996).
174 On the resulting electrical resistivity sections, total gradient computations were implemented to
175 detect marked depth and lateral variations and highlight the distribution and continuity of the soil
176 material. To constrain data interpretation, tests on the electrical resistivity of the soil material were
177 carried out on site in an uncovered soil outcrop (approximately 1.5 x 0.3 m) with a single
178 quadrupole with 0.25-0.30- and 0.40-m electrode spacing and eight array configurations of current
179 and potential electrode positions. The results were statistically analysed to retrieved average
180 reference values of the electrical resistivity of the target material.

181 Ten ground penetrating radar (GPR) profiles (Fig. 1) were complementary acquired with a 500-
 182 MHz antenna controlled by an IDS K2 digital acquisition unit. GPR traces were acquired for a total
 183 time of 100 ns and 512 samples per trace respectively. Ublox EVK-5T GPS was used to track each
 184 survey position. The average distance between subsequent traces resulted in 0.025 m along each
 185 line. A standard data processing sequence was carried out in Reflexw software (Sandmeier),
 186 involving: i) dewow, to reduce very low frequency components; ii) band-pass Butterworth filtering
 187 around the central frequency of each antenna; iii) move start time, to remove the delay introduced
 188 by the system; iv) time cut at 50 ns, to reduce the trace length after a check on the deterioration of
 189 the S/N ratio with time (depth); v) manual gain to recover trace amplitude with time (depth); vi)
 190 background removal to reduce the effect of horizontal banding in the radargrams.

191 Local rare diffraction hyperbola in the radargrams were fitted with a velocity of 0.1 m/ns. To apply
 192 this value for time-to-depth conversion, the medium velocity (v) was additionally estimated by the
 193 Complex Refractive Index Method (CRIM, Birchak et al., 1974; Wharton et al., 1980), following:

$$194 \sqrt{\epsilon_S} = (1 - \varphi) \sqrt{\epsilon_m} + \varphi S \sqrt{\epsilon_w} + \varphi (1 - S) \sqrt{\epsilon_a} \quad (2)$$

195 and

$$196 v = \frac{c}{\sqrt{\epsilon_S}} \quad (3)$$

197 where ϵ_S , ϵ_m , ϵ_w and ϵ_a are the relative dielectric permittivities of soil, soil matrix, pore water and
 198 air respectively, φ is the soil porosity, S is the degree of water saturation and $c=3 \cdot 10^8$ m/s
 199 (electromagnetic wave velocity in vacuum). In Equation 2, $\epsilon_a=1$, $\epsilon_w=77.8$ (from GPR measurements
 200 on the water of a nearby pond; Colombo et al., 2018) and $\epsilon_m=7$ (from average reference values of
 201 similar loamy sandy soils, e.g., Daniels, 2004). Soil porosity φ was indirectly estimated from
 202 density measurements in the range 0.5 to 0.6. Moist (unsaturated) conditions were present on site
 203 during GPR acquisitions. A variable S , between 0.2 and 0.4, was consequently considered in the
 204 computation. Using these parameters, average $\epsilon_S=9.3$ and $v=0.10$ m/ns were obtained for time-to-
 205 depth conversion. The approximate wavelength of a 500-MHz GPR signal in this material is

206 consequently 0.2 m, meaning approximately 0.1 m of vertical resolution (half wavelength) in the
207 investigated medium.

208

209 **3 Results and interpretation**

210 **3.1. Soil profiles characteristics**

211 Below a 10-60 cm thick stony/blocky layer (blockfields and blockstreams, respectively on flat
212 surfaces or on gentle slopes), the profiles were characterized by thick (between 30 and 65 cm) and
213 continuous dark A horizons with subangular-blocky, platy or granular structure (Table 1, Fig. 2, 3
214 and 4). These horizons were characterized by few roots and an extremely weak biogenic structure,
215 where present, and they were classified as umbric horizons according to WRB. Below the umbric
216 horizons, cambic Bw ones were often developed although discontinuous, characterized by brown
217 colour and well-expressed subangular-blocky structure (Table 1, Fig. 2, 3 and 4). Cryoturbation
218 features, such as inclusions of surface A materials at depth and convolutions and block
219 displacement above wedges, were often observed within the profiles; thick, dense silt caps were
220 also observed on the upper faces of stone fragments. The soil profiles were classified as Skeletic
221 Umbrisol (Arenic, Turbic), according to FAO (2014).

222

223 **3.2 Soils physical and chemical properties**

224 The soil texture was generally loamy sandy or sandy loamy, with a substantial prevalence of sand
225 (77% on average) compared to silt (20%) and clay (3%) fractions (Tab. 1). The clay fraction was
226 composed of ca. 60% quartz, 20% mica/illite, 10% chlorite, 10% plagioclase and other minerals in
227 traces (not shown). pH values were extremely to moderately acidic, ranging between 4.3 and 5.9.
228 TOC content spanned from 0 to over 20 g*kg⁻¹, reaching maximum values in A horizons, while TN
229 values were very low in all the samples. The TOC/TN ratio ranged between 7 and 20, reaching
230 maximum values in the A horizons.

231 Considering the overall C-STOCK_{tot} of each sector within the profiles (Table 2, Fig. 2, 3 and 4), in
232 P1 the values ranged between 0.7 and over 5 kg*m⁻², reaching minimum and maximum values in
233 sector C and A respectively; in the profile P2 the values spanned from 1.12 to approx. 3 kg*m⁻²
234 reaching minimum values in sector D and maximum in sector F; the C-STOCK_{tot} of P3 reached the
235 minimum value of 2.17 kg*m⁻² in sector K and a maximum of 3.30 in kg*m⁻² in the sector I.

236

237 **3.3 Geophysical investigation**

238 Results obtained from the long ERT line (ERT3 in Fig. 5a) provided a non-homogeneous electrical
239 resistivity distribution in the plateau bedrock. The deepest values (5-7 kΩ m in the line centre below
240 5-m depth, yellow in Fig. 5a) were interpreted as representative of compact bedrock. Higher
241 resistivities (>7 kΩ m, green in Fig. 5a) were depicted at shallower depths, reaching values of 15
242 kΩ m in proximity of the fractured overhanging rock cliff delimiting the plateau eastern edge.
243 These values were related to variable fracturing conditions of the shallow bedrock, increasing
244 towards E and NE. Relatively low electrical resistivity values, also considering the lithology of the
245 area and its fracturing conditions, pointed towards the absence of relevant bodies of permafrost in
246 the investigated area (cf., Kneisel, 2006).

247 Above the fractured bedrock, all the short ERT lines revealed the presence of a distinct and
248 discontinuous layer with variable thickness under the stony cover, with resistivity values lower than
249 5 kΩ m (red in Fig. 5, b to d). Separated measurements acquired on an uncovered soil outcrop
250 showed resistivity values in the range 2.9-4.2 kΩ m for the soils of interest, with an average of 3.6
251 kΩ m over 24 tests with different array spacing and electrode configuration. Consequently, this
252 shallow layer was interpreted as representative of the soil presence under the periglacial cover.

253 The GPR profiles depicted a complex stratigraphy in the first meters of depth. Exemplificative
254 results are reported in Fig. 6 for the GPR profiles acquired along the ERT lines of Fig. 5. Processed
255 radargrams were visually interpreted as shown in Fig. 6a. In the shallower part of each section, GPR
256 reflections appear as laterally continuous, smooth and sub-horizontal, likely due to the soil presence

257 (s in Fig. 6a). Below this layer, intricate patterns of discontinuous GPR reflections are conversely
258 present, more steeply dipping in different directions. This layer (t in Fig. 6a) possibly corresponds
259 to the transition between soil and bedrock. The chaotic arrangement of soil material and debris
260 resulting from the fractured bedrock may have generated this complex GPR response. At depths
261 higher than 1 m, GPR reflections show again a more homogeneous lateral continuity, possibly
262 indicating the bedrock presence (b in Fig. 6a).

263 Given the difficulty and subjectivity in manually picking the soil bottom from GPR sections (Fig. 6,
264 b, d and f), ERT results (Fig. 5) were transformed in total gradient sections of electrical resistivities.
265 The gradient maxima in each section were then automatically picked and interpreted as objective
266 markers of the presence of a sharp vertical and lateral contrast between soil and surrounding
267 materials and consequently used to estimate the average soil thickness in the plateau. Results are
268 shown in Fig. 6 (c, e and g) in comparison with manual picking performed on GPR sections.
269 Electrical resistivity gradient maxima generally fall within the transition layer (Fig. 6a) depicted in
270 GPR results, providing a rough estimate of the soil bottom interface. The soil presence was detected
271 by both geophysical methods within the first meter of depth of all the investigated lines.

272

273 **4 Discussion**

274 **4.1 Soil properties and carbon stocks**

275 The opening of trenches revealed the unexpected presence of complex and well-developed soils
276 (Umbrisols) under the stony cover, with convolutions and inclusions of different materials, as a
277 result of intense cryoturbation processes (Bockheim and Tarnocai, 1998). Despite the strong
278 geomorphic activity characterizing this periglacial area, the observed soils were extremely well
279 developed, particularly inside periglacial landforms (blockfields and blockstreams). Considering the
280 remarkable thickness of A horizons (up to 60 cm), these soils resulted also more developed than the
281 surrounding and vegetated soils at similar or lower elevation, where weakly developed and shallow

282 Skeletic Regosols, Cambisols or Umbrisols (e.g., Magnani et al., 2017) with thinner A horizon (up
283 to 25-30 cm) were common. The textural class as well as the pH values were comparable to those
284 found in the surrounding soils under snowbed vegetation (e.g., Magnani et al., 2017).
285 Considering the absence of a significant vegetation cover on the plateau, the high elevation and the
286 presence of the thick stony cover, the estimated total carbon stock for each sector was surprisingly
287 high. Overall, the results were comparable to carbon stock values reported for high-elevation,
288 cryoturbated soils in the Aosta Valley, although generally covered by alpine tundra, for which
289 values around 2-3 kg*m⁻² (D'Amico et al., submitted) were reported. The values were also in the
290 range reported for other vegetated soils in Alpine tundra ecosystems (Bockheim and Munroe,
291 2014). However, our results, in particular from P1, despite the lack of vegetation, were also in the
292 normal range of carbon stock values from moderately developed forest or heath soils in the Aosta
293 Valley, such as Entic Podzols (D'Amico et al., submitted), and to those reported by Chiti et al.
294 (2012) for forest ecosystems in Spain, or for mountain boreal forests in North America (Hoffmann
295 et al., 2014). In addition, on Italian Alps, very few works reported similar soils with C-rich A
296 horizons at high elevation (around 3000 m a.s.l.) (e.g., Baroni et al., 1996).

297

298 **4.2 Soil distribution, depth and subsurface morphology of the plateau**

299 Geophysical investigations confirmed the widespread presence of soils on the whole plateau.
300 Considering the soil texture, the measured electrical resistivity values (2-5 kΩ m) may appear
301 unusually high for field tests carried out in moist (but unsaturated) conditions on these materials.
302 Since the presence of minerals having relevant surface conductivity was found to be almost
303 negligible (i.e. illite and chlorite are less than 1% of the total solid matrix), a rough check on the
304 expected soil electrical resistivity ρ_S can be performed following Archie's law (Archie, 1942):

305
$$\rho_S = a \frac{\rho_w}{\varphi^{m_S k}} \quad (4),$$

306 where ρ_w is pore water resistivity (around 100 Ω m, i.e. moisture mainly due to precipitation and
307 shallow seepage), $a=1$ and $m=1.4$ are Archie's coefficients for non-consolidated sediments (Archie,
308 1942; Friedman, 2005), ϕ is the soil porosity (0.5 to 0.6), S is the degree of water saturation and k
309 coefficient can be assumed equal to 2 for $S>0.1$. Applying Equation 4, retrieved ρ_s values are in the
310 range 1.3-6.5 k Ω m for S between 0.2 and 0.4, thus additionally confirming the obtained electrical
311 resistivity values.

312 Thanks to the electrical resistivity gradient maxima analyses, the soil bottom was recognized at
313 depths ranging from 26 to 88 cm, for an average of 47 cm over the five short ERT lines. In general,
314 higher depths (and soil thicknesses) were identified in the eastern part of the plateau (ERT2 in Fig.
315 1), close to the chair lift station, in presence of a more fractured underlying bedrock and below a
316 particularly coarse stone cover. By contrast, the lowest depths were found in the grassy area on the
317 northern side of the plateau, where periglacial blockfields/blockstreams are absent (ERT6 in Fig. 1).
318 A decrease in soil thickness was also observed close to the rock outcrops present in the plateau.
319 Even if ERT surveys had lower vertical resolution with respect to GPR profiles, soil depth and
320 thickness estimations from electrical resistivity gradient maxima were straightforward and provided
321 a less subjective estimation in these complex subsurface settings.

322 Considering the remarkable thickness of soil layer and its wide distribution, it is possible to assume
323 that the overall C-stock of the plateau may be higher than estimated. In particular, the southern and
324 south-western portions of the plateau are covered by a particularly coarse and thick block cover,
325 which resembles the eastern part where the soil thickness and C stocks are larger. In addition,
326 although not expressed in the results, a negative relation between soil organic carbon content and
327 resistivity was detected.

328

329 **5 Conclusion and perspectives**

330 During the operational activities for a new chair lift construction at the Stolenberg Plateau, the
331 opening of soil trenches revealed, unexpectedly, the presence of extremely well-developed soils

332 under a thick stony cover consisting of periglacial blockfields and blockstreams. These soils,
333 classified as Umbrisol, were characterized by surprisingly high C stocks, comparable to alpine
334 tundra or even forest soils, despite the lack of vegetation and the presence of the stony cover. The
335 application of non-invasive geophysical methods revealed that these hidden soils were widespread
336 on the plateau under the stony cover, with a mean thickness around 50 cm, that generally increase
337 where the periglacial features were more expressed (up to ca. 90 cm).

338 These C-rich soils, without vegetation and covered by periglacial landforms, may represent a
339 unique pedoenvironment suggesting new perspective on the actual C stocks in high-elevation
340 ecosystems, which are probably underestimated. In addition, the origin of these C-rich soils below
341 blockstreams and blockfields, apparently in contrast with present day condition, may be of great
342 relevance for unravelling the history of the high-elevation landscape of the Monte Rosa alpine area.
343 For instance, they could be buried paleosols below moving stone layers, retaining therefore
344 information about past climate. An alternative explanation could also be related to reduced
345 decomposition of organic matter associated with the cooling effect caused by the stone cover. A
346 more precise characterization of the organic matter, its age and species has indeed to be performed
347 by further studies in the area.

348

349 **Acknowledgements**

350 This study was supported by European Regional Development Fund in Interreg Alpine Space
351 project Links4Soils (ASP399): Caring for Soil—Where Our Roots Grow. (<http://www.alpinespace.eu/projects/links4soils/en/the-project>). Many thanks to Monterosa Ski Resort (project stakeholder)
352 for providing logistical support.
353

- 355 Alberto, W., Palomba, M., Perotti, L., 2018. SMART GROUND project test-sites topographic and
356 morphologic characterization: Instruments and methodologies. *Rendiconti Online Società Geologica*
357 *Italiana* 46, 107–114.
- 358 Allred B.J., Daniels J.J., Ehsani M.R., 2008. *Handbook of Agricultural Geophysics*. CRC Press Taylor Francis
359 Group, Boca Raton.
- 360 Andre F., van Leeuwen C., Saussez S., van Durmen R., Bogaert P., Moghadas D., de Resseguier L., Delvaux B.,
361 Vereecken H.; Lambot S., 2012. High-resolution imaging of a vineyard in south of France using ground
362 penetrating radar, electromagnetic induction and electrical resistivity tomography. *Journal of Applied*
363 *Geophysics*, 78: 113–122.
- 364 Archie, G.E., 1942. The electrical resistivity log as an aid in determining some reservoir characteristics.
365 *Trans. Am. Inst. Mech. Eng.* 146, 54–67.
- 366 Arteaga, G.Á., Calderón, N.G., Krasilnikov, P.V., Sedov, S.N., Targulian, V.O., Rosas, N.V., 2008. Soil
367 altitudinal sequence on base-poor parent material in a montane cloud forest in Sierra Juárez,
368 Southern Mexico. *Geoderma* 144, 593–612.
- 369 Ballantyne, C.K., Matthews, J.A., 1982. The development of sorted circles on recently deglaciated terrain,
370 Jotunheimen, Norway. *Arctic and Alpine Research* 14, 341–354.
- 371 Baroni, C., Orombelli, G., 1996. The Alpine “Ice-man” and Holocene Climatic Change. *Quat. res.* 46, 78–83.
372 <https://doi.org/10.1006/qres.1996.0046>
- 373 Batjes, N.H., 1996. Total carbon and nitrogen in the soils of the world. *Eur J Soil Science* 47, 151–163.
374 <https://doi.org/10.1111/j.1365-2389.1996.tb01386.x>
- 375 Birchak, J.R., Gardner, C.G., Hipp, J.E., and Victor, J.M., 1974. High dielectric constant microwave probes for
376 sensing soil moisture: *Proc. IEEE*, 62, 93–98.
- 377 Biskaborn, B.K., Smith, S.L., Noetzli, J., Matthes, H., Vieira, G., Streletskiy, D.A., Schoeneich, P., Romanovsky,
378 V.E., Lewkowicz, A.G., Abramov, A., Allard, M., Boike, J., Cable, W.L., Christiansen, H.H., Delaloye, R.,
379 Diekmann, B., Drozdov, D., Etzelmüller, B., Grosse, G., Guglielmin, M., Ingeman-Nielsen, T., Isaksen,
380 K., Ishikawa, M., Johansson, M., Johannsson, H., Joo, A., Kaverin, D., Kholodov, A., Konstantinov, P.,
381 Kröger, T., Lambiel, C., Lanckman, J.-P., Luo, D., Malkova, G., Meiklejohn, I., Moskalenko, N., Oliva,
382 M., Phillips, M., Ramos, M., Sannel, A.B.K., Sergeev, D., Seybold, C., Skryabin, P., Vasiliev, A., Wu, Q.,
383 Yoshikawa, K., Zheleznyak, M., Lantuit, H., 2019. Permafrost is warming at a global scale. *Nat*
384 *Commun* 10, 264. <https://doi.org/10.1038/s41467-018-08240-4>
- 385 Bockheim, J.G., Munroe, J.S., 2014. Organic Carbon Pools and Genesis of Alpine Soils with Permafrost: A
386 Review. *Arctic, Antarctic, and Alpine Research* 46, 987–1006. [https://doi.org/10.1657/1938-4246-](https://doi.org/10.1657/1938-4246-46.4.987)
387 [46.4.987](https://doi.org/10.1657/1938-4246-46.4.987)
- 388 Bockheim, J.G., Tarnocai, C., 1998. Recognition of cryoturbation for classifying permafrost-affected soils.
389 *Geoderma* 81, 281–293.
- 390 Bojko, O., Kabala, C., 2017. Organic carbon pools in mountain soils — Sources of variability and predicted
391 changes in relation to climate and land use changes. *CATENA* 149, 209–220.
392 <https://doi.org/10.1016/j.catena.2016.09.022>
- 393 Boone R.D., Grigal D.F., Sollins P., Ahrens R.J., Armstrong, D.E., 1999. Soil sampling, preparation, archiving,
394 and quality control. In: Robertson G.P., Coleman D.C., Bledsoe C.S., Sollins P., (eds) *Standard soil*
395 *methods for long-term ecological research*. Oxford University Press, New York, pp 3–28.
- 396 Carrivick, J.L., Smith, M.W., Quincey, D.J., 2016. *Structure from Motion in the Geosciences*. John Wiley &
397 Sons, Ltd, Chichester, UK.
- 398 Celi, L., Rosso, F., Freppaz, M., Agnelli, A., Zanini, E., 2010. Soil Organic Matter Characteristics in Sporadic
399 Permafrost-affected Environment (Creux du Van, Switzerland). *Arctic, Antarctic, and Alpine Research*
400 42, 1–8. <https://doi.org/10.1657/1938-4246-42.1.1>
- 401 Cheng, H., Bai, R., Li, K., Zhao, C., Sun, S., Li, M., 2012. Study of loss or gain of soil organic carbon in Da’an
402 region, Jilin Province in China. *Journal of Geochemical Exploration* 112, 272–275.
- 403 Colombo, N., Sambuelli L., Comina C., Colombero C., Giardino M., Gruber S., Viviano G., Vittori Antisari L.
404 and Salerno F., 2018. Mechanisms linking active rock glaciers and impounded surface water

405 formation in high-mountain areas. *Earth Surface Processes and Landforms*, 43(2), 417-431. DOI:
406 10.1002/esp.4257

407 D'Amico, M., Gorra, R., Freppaz, M., 2015. Small-scale variability of soil properties and soil-vegetation
408 relationships in patterned ground on different lithologies (NW Italian Alps). *CATENA* 135, 47–58.
409 <https://doi.org/10.1016/j.catena.2015.07.005>

410 Daniels, D.J., 2004. *Ground Penetrating Radar*. 2nd edition. Radar, Sonar, Navigation and Avionics Series 15,
411 Institute of Electrical Engineers, London, UK.

412 Directive, H., 1992. Council Directive 92/43/EEC of 21 May 1992 on the conservation of natural habitats and
413 of wild fauna and flora. *Official Journal of the European Union* 206, 7–50.

414 Dong, C., 1999. PowderX: Windows-95 based program for powderX-ray diffraction data processing. *J Appl*
415 *Crystallogr.* 32:838.

416 Doolittle, J.A., Collins M.E., 1995. Use of soil information to determine application of ground penetrating
417 radar. *Journal of Applied Geophysics*, 33: 101–108.

418 Léger, E., Dafflon B., Soom, F., Peterson J., Ulrich C., Hubbard, S., 2017. Quantification of Arctic Soil and
419 Permafrost Properties Using Ground-Penetrating Radar and Electrical Resistivity Tomography
420 Datasets, in *IEEE Journal of Selected Topics in Applied Earth Observations and Remote Sensing*, vol.
421 10, no. 10, pp. 4348-4359. doi: 10.1109/JSTARS.2017.2694447

422 Novàková, E., Karous, M., Zajiček, A., Karousovà, M., 2013. Evaluation of ground penetrating radar and
423 vertical electrical sounding methods to determine soil horizons and bedrock at the locality Dehtáře.
424 *Soil & Water Res.*, 8 (3), pp. 105-112

425 FAO, 2014. *World reference base for soil resources 2014: international soil classification system for naming*
426 *soils and creating legends for soil maps*. FAO, Rome.

427 Freppaz, M., Viglietti, D., Balestrini, R., Lonati, M., Colombo, N., 2019. Climatic and pedoclimatic factors
428 driving C and N dynamics in soil and surface water in the alpine tundra (NW-Italian Alps). *NC* 34, 67–
429 90. <https://doi.org/10.3897/natureconservation.34.30737>

430 Friedman, S.P., 2005. Soil properties influencing apparent electrical conductivity: a review. *Comput.*
431 *Electron. Agric.* 46, 45–70.

432 Gerdol, R., Smiraglia, C., 1990. Correlation between vegetation pattern and microtopography in periglacial
433 areas of the Central Alps. *Pirineos* 135, 13–28.

434 FAO, 2016. *Guidelines for soil description*, 4th ed. ed, 2006. . Food and Agriculture Organization of the
435 United Nations, Rome.

436 Hagedorn, F., Mulder, J., Jandl, R., 2010. Mountain soils under a changing climate and land-use 5.

437 Hoffmann, U., Hoffmann, T., Johnson, E.A., Kuhn, N.J., 2014. Assessment of variability and uncertainty of
438 soil organic carbon in a mountainous boreal forest (Canadian Rocky Mountains, Alberta). *Catena* 113,
439 107–121.

440 Islam A.K.M.E., Lotse, E.G. 1986. Quantitative mineralogical analysis of some Bangladesh soils with X-ray,
441 ion exchange and selective dissolution techniques. *Clay Miner.* 21:31–42.

442 Otto, J.C., Sass, O., 2006. Comparing geophysical methods for talus slope investigations in the Turtmann
443 valley (Swiss Alps), *Geomorphology*, Volume 76, Issues 3–4, 257-272.
444 <https://doi.org/10.1016/j.geomorph.2005.11.008>.

445 Kneisel, C., Hauck, C., Fortier, R. and Moorman, B., 2008. Advances in geophysical methods for permafrost
446 investigations. *Permafrost Periglac. Process.*, 19: 157-178. doi:10.1002/ppp.616

447 Kneisel, C., 2006. Assessment of subsurface lithology in mountain environments using 2D resistivity
448 imaging. *Geomorphology*, 80(1-2), 32-44.

449 Knowles, J.F., Blanken, P.D., Lawrence, C.R., Williams, M.W., 2019. Evidence for non-steady-state carbon
450 emissions from snow-scoured alpine tundra. *Nat Commun* 10, 1306. [https://doi.org/10.1038/s41467-](https://doi.org/10.1038/s41467-019-09149-2)
451 [019-09149-2](https://doi.org/10.1038/s41467-019-09149-2).

452 Leifeld, J., Zimmermann, M., Fuhrer, J., Conen, F., 2009. Storage and turnover of carbon in grassland soils
453 along an elevation gradient in the Swiss Alps. *Global Change Biology* 15, 668–679.
454 <https://doi.org/10.1111/j.1365-2486.2008.01782.x>

455 Loke, M.H., Barker, R.D., 1996. Rapid least-squares inversion of apparent resistivity pseudosections by a
456 quasi-Newton method. *Geophysical Prospecting*, 44, 131-152 .

457 Magnani, A., Viglietti, D., Godone, D., Williams, M.W., Balestrini, R., Freppaz, M., 2017. Interannual
458 Variability of Soil N and C Forms in Response to Snow—Cover duration and Pedoclimatic Conditions
459 in Alpine Tundra, Northwest Italy. *Arctic, Antarctic, and Alpine Research* 49, 227–242.
460 <https://doi.org/10.1657/AAAR0016-037>

461 McClymont, A. F., Hayashi, M., Bentley, L. R., Muir, D., Ernst, E., 2010. Groundwater flow and storage within
462 an alpine meadow-talus complex, *Hydrol. Earth Syst. Sci.*, 14, 859–872, [https://doi.org/10.5194/hess-](https://doi.org/10.5194/hess-14-859-2010)
463 [14-859-2010](https://doi.org/10.5194/hess-14-859-2010).

464 Mollaret, C., Hilbich, C., Pellet, C., Flores-Orozco, A., Delaloye, R., Hauck, C., 2019. Mountain permafrost
465 degradation documented through a network of permanent electrical resistivity tomography sites.
466 *The Cryosphere* 13, 2557–2578.

467 Prietzel, J., Christophel, D., 2014. Organic carbon stocks in forest soils of the German Alps. *Geoderma* 221–
468 222, 28–39. <https://doi.org/10.1016/j.geoderma.2014.01.021>

469 Samouelian, A., Cousin, I., Tabbagh, A., Bruand, A., Richard, G., 2005. Electrical resistivity survey in soil
470 science: A review, *Soil Tillage Res.*, 83, 173 – 193, doi:10.1016/j.still.2004.10.004.

471 Schroter, D., 2005. Ecosystem Service Supply and Vulnerability to Global Change in Europe. *Science* 310,
472 1333–1337. <https://doi.org/10.1126/science.1115233>

473 Schuur, E.A.G., Abbott, B.W., Bowden, W.B., Brovkin, V., Camill, P., Canadell, J.G., Chanton, J.P., Chapin,
474 F.S., Christensen, T.R., Ciais, P., Crosby, B.T., Czimczik, C.I., Grosse, G., Harden, J., Hayes, D.J.,
475 Hugelius, G., Jastrow, J.D., Jones, J.B., Kleinen, T., Koven, C.D., Krinner, G., Kuhry, P., Lawrence, D.M.,
476 McGuire, A.D., Natali, S.M., O’Donnell, J.A., Ping, C.L., Riley, W.J., Rinke, A., Romanovsky, V.E., Sannel,
477 A.B.K., Schädel, C., Schaefer, K., Sky, J., Subin, Z.M., Tarnocai, C., Turetsky, M.R., Waldrop, M.P.,
478 Walter Anthony, K.M., Wickland, K.P., Wilson, C.J., Zimov, S.A., 2013. Expert assessment of
479 vulnerability of permafrost carbon to climate change. *Climatic Change* 119, 359–374.
480 <https://doi.org/10.1007/s10584-013-0730-7>

481 Smith, M.V., Carrivick J.L., Quincey D.J., 2015. Structure from motion photogrammetry. *Physical Geography*
482 40, 247–275.

483 Van Reeuwijk, L.P., 2002. Procedures for Soil Analysis. Technical Paper n. 9.

484 Wharton, R.P., Hazen, G.A., Rau, R.A., Best, D.L., 1980. Electromagnetic propagation logging—advances in
485 technique and interpretation: *Soc. Petr. Eng.*, 55th Annual Technical Conference, Paper 9267.

486 Zollinger, B., Alewell, C., Kneisel, C., Meusbürger, K., Gärtner, H., Brandová, D., Ivy-Ochs, S., Schmidt,
487 M.W.I., Egli, M., 2013. Effect of permafrost on the formation of soil organic carbon pools and their
488 physical–chemical properties in the Eastern Swiss Alps. *CATENA* 110, 70–85.
489 <https://doi.org/10.1016/j.catena.2013.06.010>

490

491 Figures

492 Figure 1: Location of the study area in the NW Italian Alps (www.pcn.minambiente.it), and overview of the study area
493 (orthoimage Piemonte Region, year 2010) and photo (M. D'Amico). Solid and dashed lines indicate ERT and GPR profiles,
494 respectively. Yellow lines indicate the profiles showed and discussed in the manuscript. Yellow circles identify the starting point
495 of each geophysical profile. Cyan polygons indicate the location of the three soil profiles (P1, P2, and P3).

496 Figure 2. Soil profile P1 with sampling points scheme (numbers) and sectors (letters) in which C-stocks were estimated.

497 Figure 3. Soil profile P2 with sampling points scheme (numbers) and sectors (letters) in which C-stocks were estimated.

498 Figure 4. Soil profile P3 with sampling points scheme (numbers) and sectors (letters) in which C-stocks were estimated.

499 Figure 5. ERT sections: (a) ERT3 (long); (b) ERT2; (c) ERT5; (d) ERT6. The location of the ERT lines is reported in figure 1. Short
500 sections are cut at 1.5-m depth.

501 Figure 6. GPR results. (a) Zoom on GPR4 section with tentative interpretation of the shallow stratigraphy: soil (s), soil-to-bedrock
502 transition (t), bedrock (b). (b, d, f) Processed radargrams for lines GPR4, GPR8, GPR5 (vertical cut at 1.5-m depth). (c, e, g) Soil
503 bottom estimation on the above sections. Comparison between the location of the electrical resistivity gradient maxima
504 computed on the ERT lines of Figure 5 (red dots) and the piking of the different layers on GPR results as shown in Figure 6a (in
505 blue, dotted line: s-t interface, dashed line t-b interface). The location of the GPR profiles is reported in Figure 1.

506

Tables

P1																
Sample number	Horizon	Munsel colour, moist	Stone fragments (%)	Clay (%)	Silt (%)	Sand (%)	Textural class	Structure	pH	TOC (g*kg ⁻¹)	TN (g*kg ⁻¹)	TOC/TN	BD (kg*m ⁻³)	TH (m)	VF	C-STOCK (kg*m ⁻²)
1	A2	10YR 3/2	30	2.81	14.54	82.65	LS	SB	4.8	19.02	0.97	20	1000	0.20	0.70	2.66
2	A1	10YR 3/2	30	2.54	14.95	82.51	LS	SB	4.4	10.77	0.80	13	1000	0.30	0.70	2.26
3	BA	10YR 3/3	40	1.59	23.25	75.16	LS	BL	4.8	4.74	0.44	11	1200	0.20	0.60	0.68
4	A1+A2	10YR 3/2	40	2.69	15.35	81.96	LS	GR	4.7	12.04	1.05	11	1000	0.30	0.60	2.17
5	A	10YR 3/2	80	2.69	14.45	82.86	LS	GR	4.4	18.58	1.47	13	1000	0.20	0.20	0.74
P2																
6	A	10YR 2/1	30	2.64	20.85	76.51	LS	SB	4.3	8.00	0.76	11	1000	0.20	0.70	1.12
7	A@	10YR 3/2	10	2.29	23.25	74.46	LS	PL/SB	5.6	20.53	1.08	19	1100	0.05	0.90	1.02
8	A2	10YR 3/3	30	1.89	18.30	79.81	LS	SB	4.7	10.95	0.79	14	1000	0.20	0.70	1.53
9	A1	10YR 3/2	70	2.54	12.09	85.37	LS	GR	4.4	11.30	1.05	11	1000	0.10	0.30	0.34
10	BC	10YR 4/4	70	1.43	27.56	71.01	SL	PL/SB	5.3	1.40	BDL	-	1200	0.20	0.30	0.10
11	CB	10YR 5/2	70	1.04	26.31	72.65	LS	SB	5.9	BDL	BDL	-	1200	0.20	0.30	0.00
12	BW	10YR 3/4	60	0.89	25.75	73.36	LS	SB	5.2	2.56	0.29	9	1200	0.20	0.40	0.25
13	A	10YR 3/2	30	4.33	24.12	71.55	SL	BL	4.8	10.94	0.77	14	1000	0.15	0.70	1.15
14	BA	10YR 3/3	50	2.84	29.25	67.91	SL	CO/PR	4.9	11.00	0.72	15	1200	0.20	0.50	1.32
15	A	10YR 3/2	10	3.89	14.00	82.11	LS	GR	4.5	7.13	0.91	8	1000	0.15	0.90	0.96
16	Silt caps	10YR 6/4	10	6.24	41.90	51.86	SL	PL	5.0	2.76	0.33	8	1300	0.03	0.90	0.10
P3																
1	A1	10YR 2/1	70	4.29	8.05	87.66	S	GR	4.9	5.62	0.45	12	1000	0.05	0.30	0.08
2	A2	10YR 3/2	5	3.24	15.60	81.16	LS	GR	4.9	8.72	0.50	17	1000	0.28	0.95	2.28
3	A2	10YR 3/2	5	4.23	15.64	80.13	LS	CO	4.9	10.47	0.70	15	1000	0.25	0.95	2.49
4	A2	10YR 3/2	20	4.84	28.24	66.93	SL	CO	4.8	7.56	0.52	14	1000	0.25	0.80	1.51
5	A2	10YR 3/2	0	4.82	20.75	74.44	SL	SG	4.7	11.82	0.69	17	1000	0.05	1.00	0.59
6	Bw	10YR 5/4	20	2.64	31.85	65.51	SL	SB	5.0	1.46	0.22	7	1200	0.25	0.80	0.35

7	BC	10YR 4/3	50	3.39	16.75	79.86	LS	SB	5.2	2.42	0.24	10	1200	0.20	0.50	0.29
8	A2	10YR 3/2	0	2.77	13.73	83.50	LS	GR	4.9	8.09	0.47	17	1000	0.02	1.00	0.16
9	BC	10YR 4/3	70	4.64	19.50	75.86	LS	PL	5.1	3.07	0.33	9	1200	0.20	0.30	0.22
10	Bw	10YR 3/4	40	3.34	19.55	77.11	LS	SB	5.2	1.65	0.21	8	1200	0.30	0.60	0.36

Table 1. Morphological, physical and chemical properties of the soil profiles. Textural class: LS=loamy sand; SL=sandy loam. Structure: SB=subangular blocky; BL=blocky; GR=granular; PL=platy; CO=columnar; PR=prismatic; SG=single grain. BDL=below detection limit.

P1			
Sector	Horizon	Sample number	C-STOCK_{tot} (kg*m⁻²)
A	A1	2	5.18
	A2	1	
	BA	3b	
B	A1+A2	4	2.85
	BA	3	
C	A	5	0.74
P2			
D	A	6	1.12
E	A1	9	2.89
	A2	8	
	A@	7	
F	A1	9	2.99
	A2	8	
	A@	7	
	BC	10	
G	CB	11	1.50
	A	13	
	Bw	12	
H	BC	10b	2.38
	A	15	
	BA	14	
	Silt caps	16	
P3			
I	A1	1	3.30
	A2	2	
	A2	5	
	Bw	6	
J	A1	1	3.02
	A2	3	
	A2	8	
	BC	7	
K	A1	1	2.17
	A2	4	
	Bw	10	
	BC	9	

Table 2. Total C-stock of the profiles for each sector.

Figure1
[Click here to download high resolution image](#)

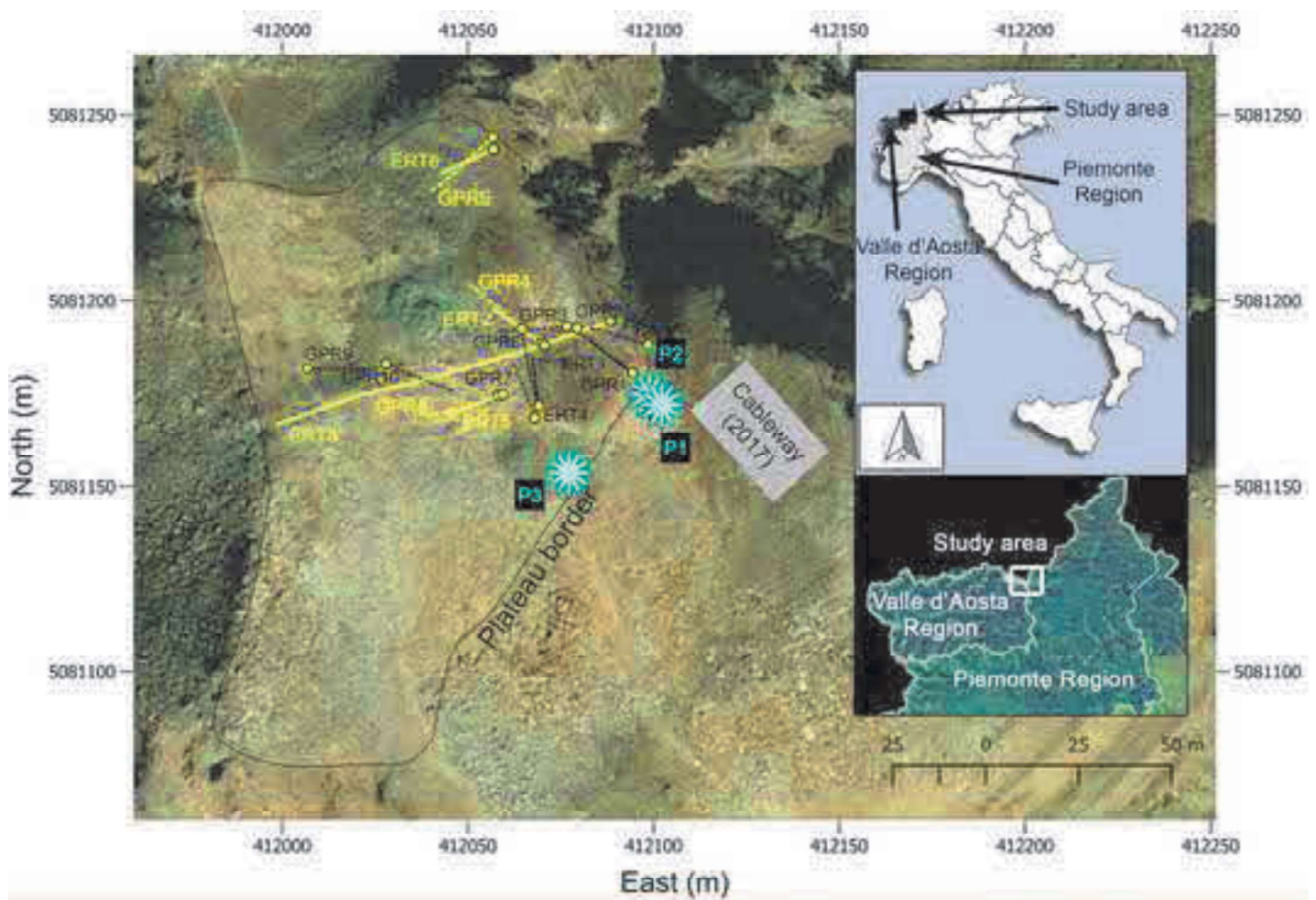


Figure2
[Click here to download high resolution image](#)

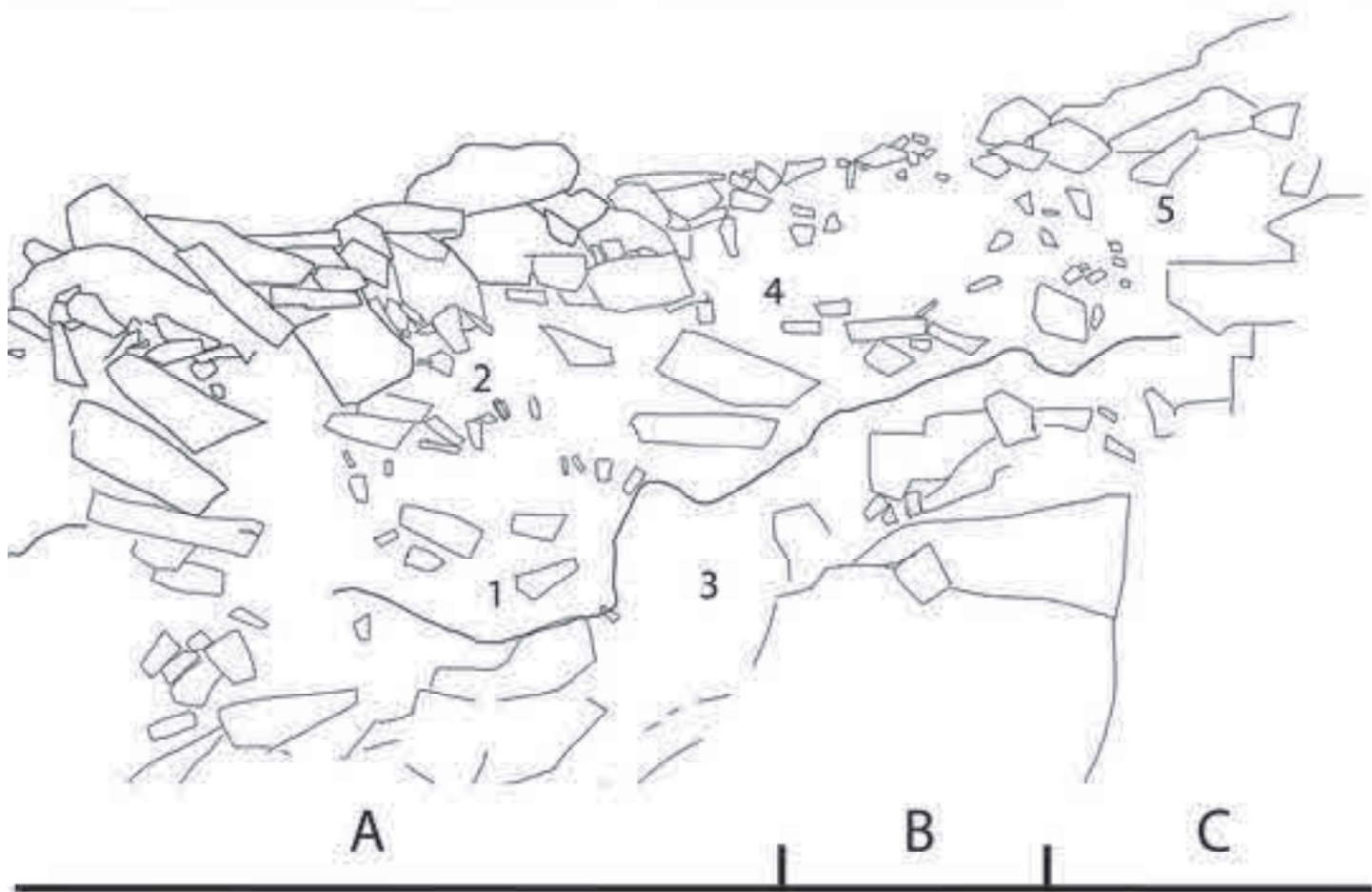


Figure3
[Click here to download high resolution image](#)

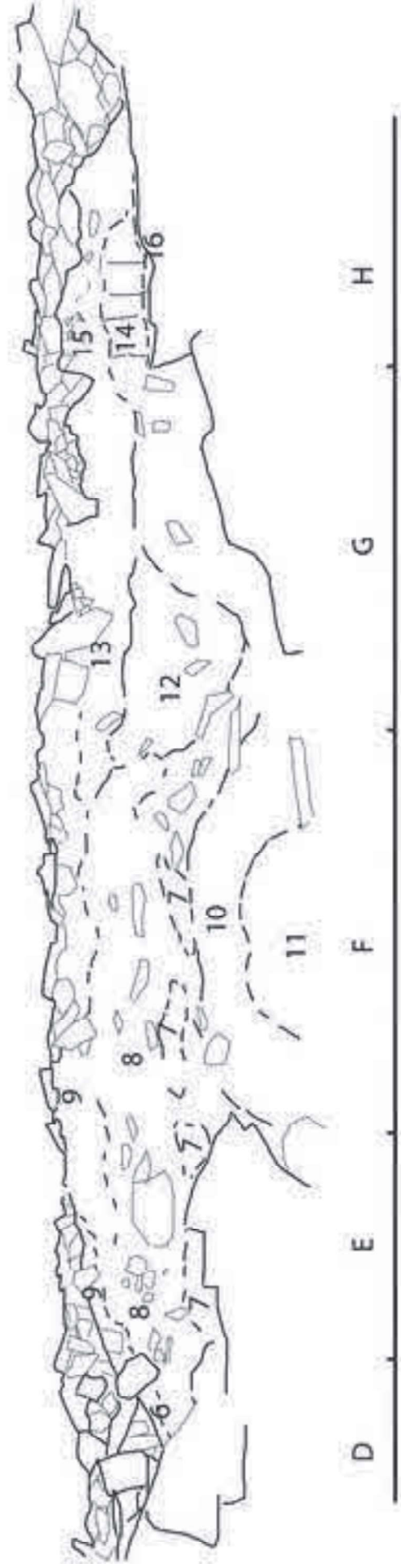


Figure 4
[Click here to download high resolution image](#)

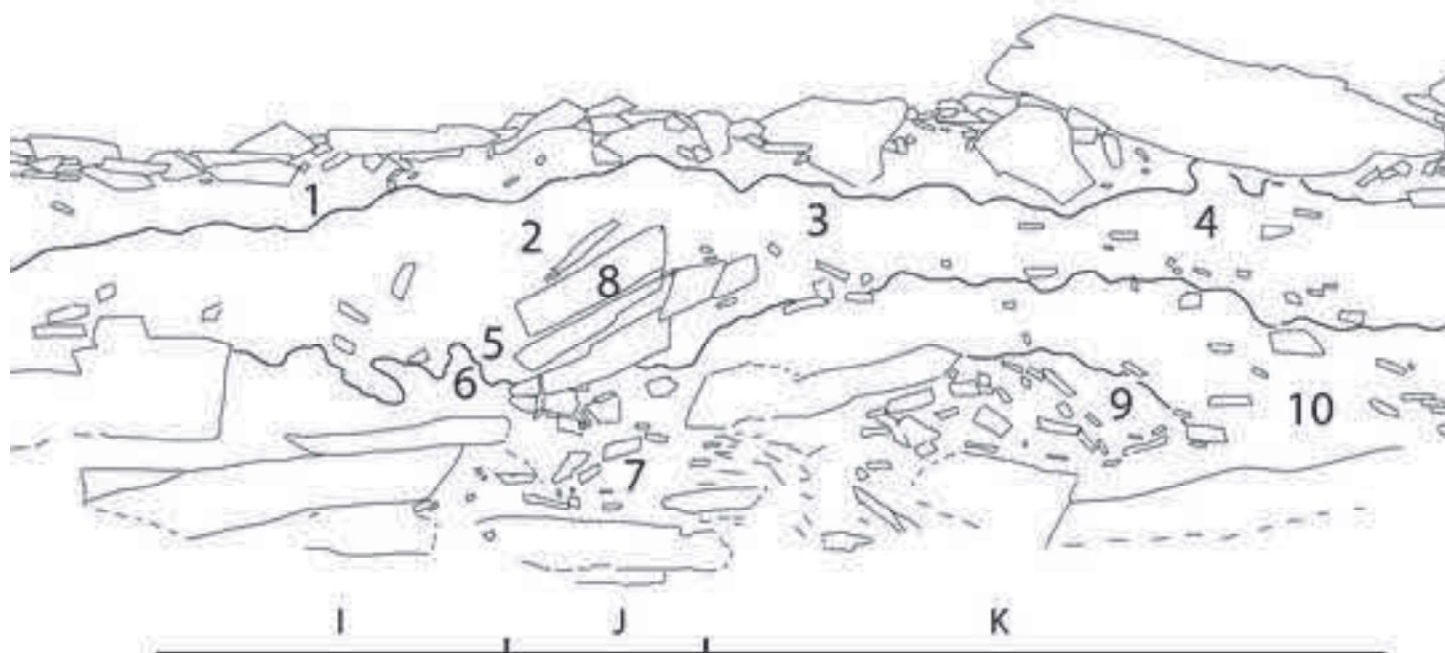
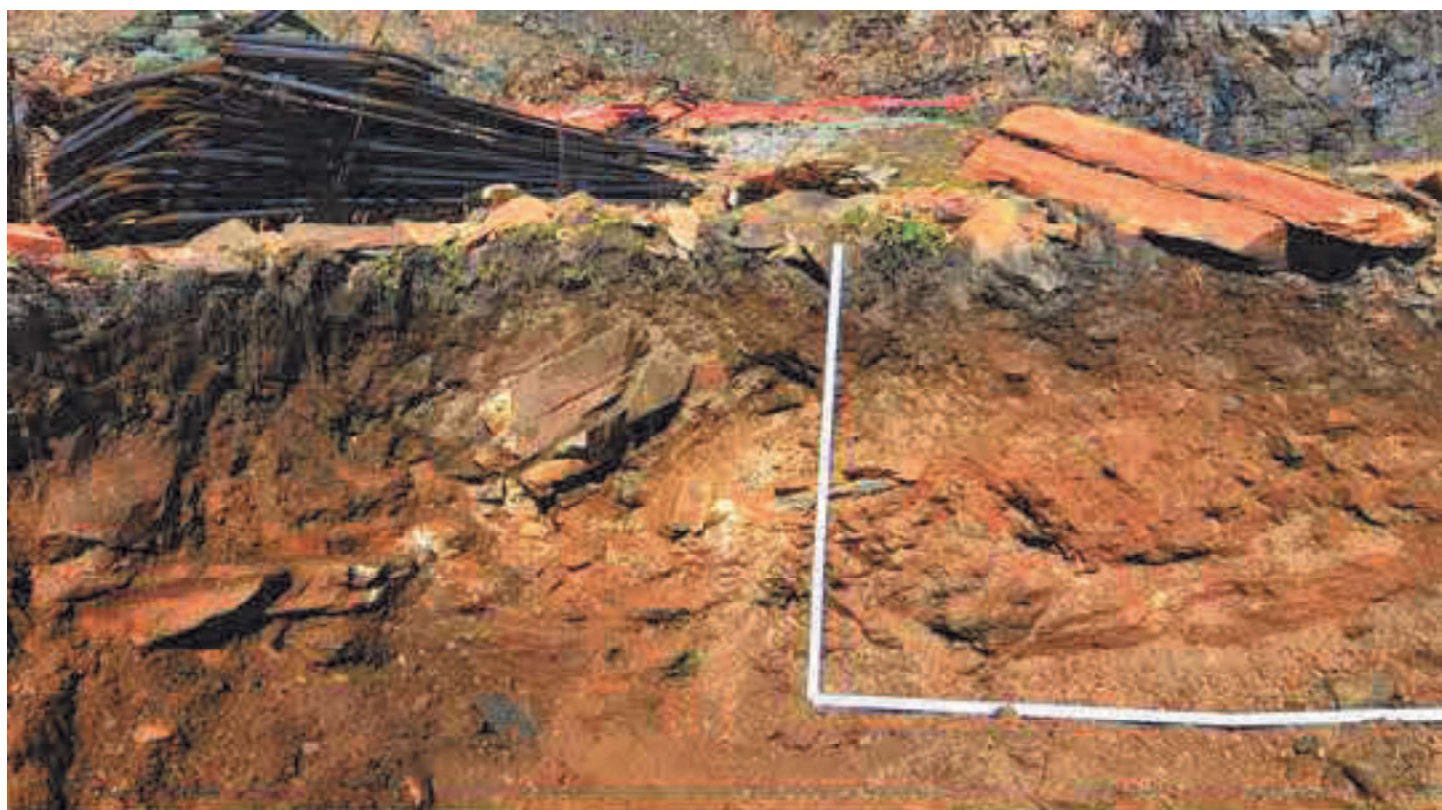


Figure 5
Click here to download high resolution image

